Boosting H_2O_2 photosynthesis by accumulating photo-electrons on carbonyl active site of polyimide covalent organic frameworks

Wenwen Chi [a], Bing Liu [a], Yuming Dong [a,*], Jiawei Zhang [a], Xinyu Sun [a], Chengsi Pan [a], Hui Zhao [a], Yujie Ling [a], Yongfa Zhu [b]

[a] International Joint Research Center for Photoresponsive Molecules and Materials, Key Laboratory of Synthetic and Biological Colloids, School of Chemical and Material Engineering, Jiangnan University, Wuxi 214122, China
[b] Department of Chemistry, Tsinghua University, Beijing 100084, China

ARTICLE INFO

ABSTRACT

The low trapping efficiency of photogenerated electrons by the targeted reduction site seriously restricts the kinetics of H_2O_2 photosynthesis via two-electron oxygen reduction reaction. Here, two polyimide covalent organic frameworks (PT-COF and PB-COF) possessing carbonyl groups with different electron-trapping capacity were elaborately designed. PB-COF with electron-rich carbonyl site presented 4.22 times improvement in H_2O_2 formation rate up to 2044 $\mu mol\ g^{-1}\ h^{-1}$, and exhibited outstanding photostability after 120 h continuous opearting. Meanwhile, solar to-chemical energy efficiency was 0.68%, representing one of advanced polymer based photocatalysts. We demonstrated electronic structure of the carbonyl active center was modulated by tuning electron attraction capability of the donor unit via increased the built-in electric field to accelerate charge separation and directional transfer. The electron-rich carbonyl site is identified to boosted H_2O_2 photosynthesis activity via reducing the *OOH binding energy. Our work offers a tailoring electron density of pre-designable active site strategy for enhanced solar-to-chemical energy conversion.

1. Introduction

The solar driven organic polymer semiconductor for artificial photosynthesis is regarded as the most promising approach for energy crisis and environmental issues [1,2]. Hydrogen peroxide (H_2O_2) is one of the most essential chemicals and valuable energy carrier, which widespread applied in a variety of fields including medical, industrial and environmental [3,4]. The global demand for hydrogen peroxide is the persistent growth [5]. Artificial photosynthesis H_2O_2 from H_2O and O_2 using renewable sunlight as the only energy input and semi-conductors photocatalyst, is an attractive route [6]. Compared to the highly energy-intensive anthraquinone process, it has the advantages of green-economic, sustainable and energy saving characteristic [7]. Recently, a burgeoning of organic semiconductors photocatalysts have developed for photosynthesis H_2O_2 [8–12]. Particularly, covalent organic frameworks (COFs) as crystalline organic materials, possesses multifarious building blocks, pre-designable framework structures, rich bondforming reactions, tunable optical and electronic properties, providing an ideal platform for photosynthesis [13–15]. Restricted by

low O_2 conversion to H_2O_2 efficiency, prevalent COF-based photo-catalysts are still far from practical implement for scalable solar-driven H_2O_2 production [16,17]. Consequently, further enhancing the H_2O_2 production efficiency of COF-based photocatalysts are highly desired to replace the unsustainable anthraquinone process [18–20].

Rationally building reaction site is considered to be crucial for enhanced photocatalytic activity [21–24]. Ideal catalytic sites not only favor O_2 adsorption and have high two-electron O_2 reduction selectivity, but also gather photogenerated electron to promote surface oxygen reduction reaction. Up to now, available active sites for two-electron reduction of O_2 include triazine, s-heptazine, pyridine, diarylamine, pyridazine, bipyridine, benzene, pyrene, thiophene and anthraquinone [25–29]. However, previously reported O_2 reduction sites suffered from the low-efficiency in trapping photogenerated electrons, seriously limiting the efficiency of H_2O_2 photosynthesis and hindering their practical application. The difference in electron-trapping capacity for reductive site affects the catalytic kinetics. Furthermore, the investigations on the tuning of electron-trapping ability for active site are still on their early stage. Possessing to excellent redox behavior, high

mechanical strength, superior photochemical and thermal stability, polyimide covalent organic frameworks (PI-COFs) presents exciting potentials in artificial photosynthesis [30,31]. Due to the strong electronegativity of oxygen atom, carbonyl groups in polyimide can be served as active center. Meanwhile, carbonyl group from polyimide has the property of absorbing and storing electrons, which not only promotes the directional migration of photogenerated electrons, but also lowers the recombination rate of carriers, further improving utilization of photogenerated electrons. Moreover, carbonyl group in imide ring is connected to donor unit via imide bond with a certain degree of conjugation, which facilitates charge transport. Therefore, carbonyl groups of PI-COFs with strong electron affinity feature can be served as trapping site to gather the electron and accelerate carrier separation [32–34], which making it desirable catalytic center for O_2 photoreduction to H_2O_2. These advantages motivates us to functionalize PI-COFs from molecular level for photocatalytic H_2O_2 production.

With these considerations in mind, we rationally constructed PI-COFs photocatalysts with highly efficient two-electron oxygen reduction reaction (2e- ORR) performance through developing different electron-trapping capacity carbonyl reductive site. For the first time, the redox carbonyl groups of pyromellitic dianhydride (PMDA) were designed as the reductive center for the effective and sustainable photosynthesis of H_2O_2. Photosynthesis H_2O_2 generation yield of 2044 μmol g^{-1} h^{-1} was achieved over PB-COF with electron-rich carbonyl site, which was 4.22 times promotion of PT-COF with the relative electron-deficient carbonyl site (484 μmol g^{-1} h^{-1}). Moreover, the accumulative yield of photosynthesized H_2O_2 reached 972.45 μmol g^{-1} after 6 h of natural sunlight irradiation, dispalying the potential practical application of PB-COF photocatalyst immobilized onto 300 cm^{-2} nonwoven fabric. Electron-rich carbonyl site has been accomplished by the robust built-in electric field to elevate charge separation and directional transfer efficiency, which contributed to enhanced photocatalysis activity. Especially, we revealed that carbonyl groups with strong electron affinity via gathering photogenerated-electron accumulation and reducing the energy barrier of the key *OOH intermediate during the 2e- ORR, thereby dramatically boosted photocatalysis activity.

2. Experimental

2.1. Synthesis of PT-COF

The PT-COF photocatalyst presented in this research was prepared by the imidization of aromatic triamines 4,4',4''-(1,3,5-triazine-2,4,6-triyl) trianiline (TAPT) with aromatic dianhydrides Pyromellitic dianhydride (PMDA). Typically, PMDA (35.4 mg, 0.15 mmol) dissolved in 0.75 mL of 1-methayl-2-pyrrolidinone (NMP) solution, then TAPT (35.4 mg, 0.10 mmol) dispersed in 0.75 mL of Mesitylene solution, then Isoquinoline (0.05 mL) was added. After being sonication with the power of 100 W for 10 min. Afterwards, the ampules were subjected to freeze-pump-thaw for three times and then put into an oven at 160 °C for 5 days. The ampules were cooled down to room temperature after the reaction, the resulting precipitate was then filtered and successively washed using DMF and THF, following Soxhlet extraction in THF for 24 h. The samples were dried under vacuum to afford PT-COF as powder (yield: ~82%).

2.2. Synthesis of PB-COF

The PB-COF photocatalyst presented in this research was prepared by the imidization of aromatic triamines 5'-(4-aminophenyl)-[1,1':3',1''-terphenyl]-4,4''-diamine (TAPB) with PMDA. Typically, PMDA (35.4 mg, 0.15 mmol) dissolved in 1.0 mL of 1,3-dimethyl-2-imidazolidinone (DMI), then TAPB (35.1 mg, 0.10 mmol) dispersed in 0.50 mL of Mesitylene solution, then Isoquinoline (0.02 mL) was added. After being sonication with the power of 100 W for 10 min. Afterwards, the ampules were subjected to freeze-pump-thaw for three times and then put into an oven at 160 °C for 5 days. The ampules were cooled down to room temperature after the reaction, the resulting precipitate was then filtered and successively washed using DMF and THF, following Soxhlet extraction in THF for 24 h. The samples were dried under vacuum to afford PB-COF as powder (yield: ~72%).

2.3. Photocatalytic H_2O_2 production

15 mg PI-COFs photocatalysts and 20 mL of deionized water were put in a square bottle (50 mL). The pure O_2 was bubbled into the suspension for 30 min in the dark. During the reaction, O_2 was kept bubbling to maintain the O_2-rich environment. A 300 W Xe lamp under simulated AM1.5 G sunlight illumination was utilized as the light source. The light average intensity is 325 mW·cm^{-2}. The H_2O_2 concentration was determined by a potassium titanium oxalate method.

2.4. Isotopic labeling experiment

^{18}O in the produced H_2O_2 was determined by converting H_2O_2 to H_2O. ^{18}O in the converted H_2O was analyzed by Liquid Water Isotope Analyzer (Los Gatos Research, USA). The conversion method was as follows: First, the collected potassium titanium oxalate-H_2O_2 complex was re-dissolved and dried; then, the potassium titanium oxalate-H_2O_2 complex was reduced by KI to convert the contained H_2O_2 species to H_2O; finally, the converted H_2O was collected by distillation and detected by Liquid Water Isotope Analyze.

3. Results

To build the excellent activity and high photostability 2D-COFs, rationally selecting building block and linkage is critical for photocatalysis. On the one hand, redox carbonyl groups of polyimide promisingly are applied as the oxygen reduction center for H_2O_2 formation, but it hasn't been explored. On the other hand, benzene group or triazine moiety has shown to serve as the water oxidation center for O_2 formation [35]. Therefore, incorporating triazine or benzene moiety into polyimide covalent organic frameworks, effectively realizes solar-driven H_2O_2 production from O_2 and H_2O system. Here, we designed and synthesized two polyimide covalent organic frameworks (2D PT-COF and 2D PB-COF) by alternating carbonyl groups of pyromellitic dianhydride (PMDA) as an extraordinary electron reservoir [36], and aromatic triamines 1,3,5-tris(4-aminophenyl) triazine (TAPT) or 1,3,5-tris(4-aminophenyl) benzene (TAPB) as electron-donating blocks linked by imide bond with superior stability (Supplementary Figs 3–4). The theoretical calculations were carried out on above PI-COFs (see calculation details in Supplementary Information). The highest occupied molecular orbital (HOMO) and the lowest unoccupied molecular orbital (LUMO) in 2D PT-COF are mainly contributed by TAPT and PMDA moiety, respectively. Whereas, HOMO and LUMO in 2D PB-COF are mainly contributed by the same TAPB and PMDA moiety, respectively. Apparently, PI-COFs with specific intermolecular charge transfer direction and the same O_2 reduction center are successfully constructed for photocatalysis.

3.1. Structural characterizations of the PI-COFs

To confirm the crystal structure of PI-COFs, powder X-ray diffraction (PXRD) measurements with structural simulation and Pawley refinement were performed. The condensation reaction of PMDA and TAPT unit will generate 2D crystalline COF with 37 Å hexagonal pore [37], termed PT-COF (Fig. 1**a**). Replacing TAPT with the same size TAPB unit also produces similar 2D crystalline COF (PB-COF) (Fig. 1**d**). Furthermore, PT-COF and PB-COF displayed identical experimental PXRD patterns, which were highly consistent with the simulated PXRD patterns of the 2D honeycomb [38]. (Figs. 1**b and** 1**e**). PB-COF showed an intense peak at 3.02° and other minor peaks at 5.23°, 6.04°, 7.99° and
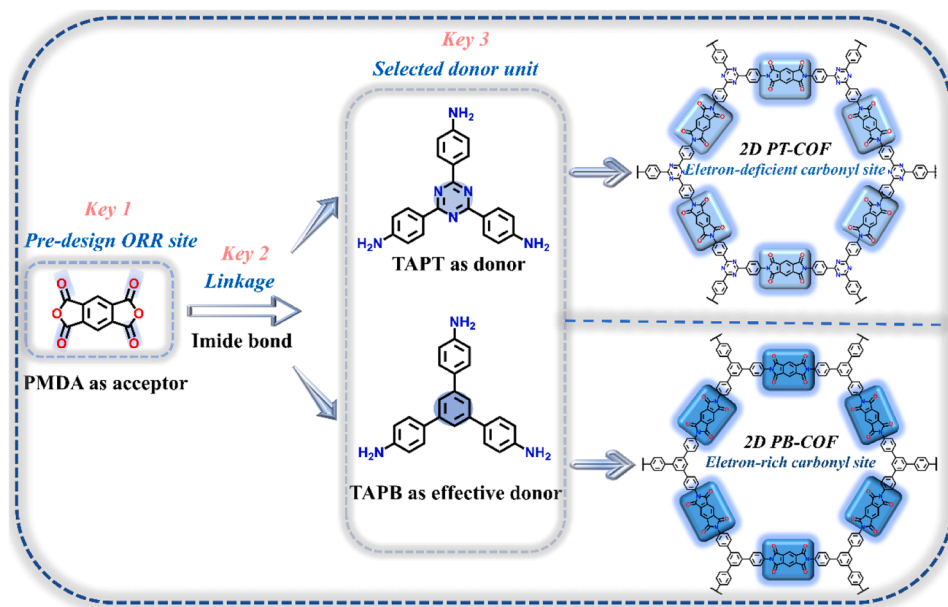
Scheme 1. Schematic for the design and synthesis of polyimide covalent organic frameworks with electron-rich carbonyl reductive site through imide condensation reaction.
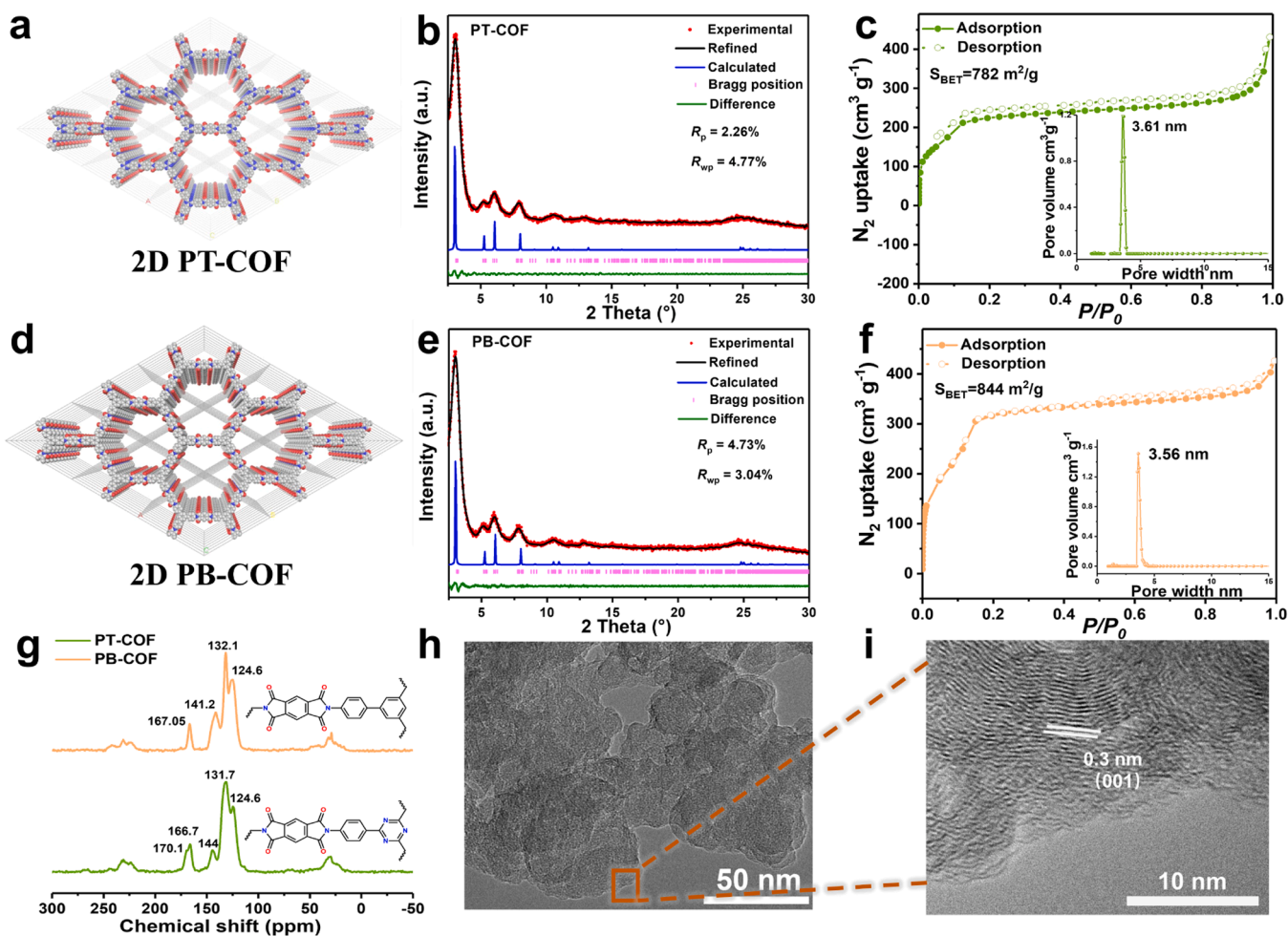
Fig. 1. (a) Front views of the proposed unit cells of AA stacking mode of PT-COF; (b) XRD patterns of experimental and simulated PT-COF; (c) N$_2$ sorption isotherms at 77 K and pore size distribution calculated by NLDFT of PT-COF; (d) Front views of the proposed unit cells of AA stacking mode of PB-COF; (e) XRD patterns of experimental and simulated PB-COF; (f) N$_2$ sorption isotherms at 77 K and pore size distribution calculated by NLDFT of PB-COF; (g) Solid state ^{13}C NMR spectra of PT-COF and PB-COF; (h) and (i) TEM and HRTEM images of PB-COF (scale bar: 50 and 10 nm).

24.80° assigned to the Bragg diffraction of the (100), (110), (200), (210) and (001) planes, respectively. (Fig. 1e) The experimental PXRD pattern of PB-COF was in agreement with the simulated PXRD pattern of the aligned AA stacking model. To verify pore diameter and predicted crystal structure of the prepared PI-COFs, nitrogen adsorption/desorption isotherms were carried out (Figs. 1c and 1f). The BET surface area of PT-COF and PB-COF was calculated to be about 782 and 844 m^2 g^{-1} based on the nitrogen adsorption/desorption isotherms, respectively. Besides, the pore diameter distribution of PI-COFs showed a major pore size of 3.61 or 3.59 nm by using the nonlocal density functional theory (NLDFT), which well matched with the pore size predicted (37 Å) from the theoretical structure. These findings provided strong support that PI-COFs with high crystallinity, large surface area and ultra-high porosity are obtained.

To assess the formation of the PI-COFs, fourier transform infrared (FT-IR), solid-state ^{13}C NMR spectroscopy and X-ray photoelectron spectroscopy (XPS) were corporately performed. The disappear of characteristic peaks for 1781 cm^{-1} (C=O group) and about 3362 cm^{-1} (N-H stretch) indicated the exist of imidized reaction (Supplementary Figs 5–6). FT-IR spectra showed absorptions at 1773.97 and 1713.64 cm^{-1} for PT-COF corresponding to asymmetric and symmetric vibrations of C=O group in imide ring; whereas peak at 1345.93 cm^{-1} for PT-COF were attributed to the stretching vibration of the N–C in imide ring. A small band at approximately 1361.3 cm^{-1} was identified the C-N-C stretching vibration of the triazine ring in PT-COF. In contrast to the spectra of PB-COF, the absorptions at 1775.12, 1725.85 and 1363.32 cm^{-1} were attributed to the asymmetric vibration of C=O, symmetric vibration of C=O and stretching vibration of N–C in imide ring, respectively [39]. The formation of the imide ring was further confirmed by solid-state ^{13}C NMR spectroscopy. As exhibited in Fig. 1g, the peak at 167.05 ppm for PB-COF, 166.71 ppm for PT-COF were assigned to the carbon of the carbonyl group [40]. Other overlapping peaks at 132.1 and 124.6 ppm for PB-COF, 131.7 and 124.6 ppm for PT-COF were well ascribed to the carbon of benzene ring [41]. Meanwhile, peak at 170.1 ppm for PT-COF was assigned to the carbon of triazine ring. XPS spectra showed that both PB-COF and PT-COF were composed of the element C, O and N element. As shown in Figure S7, the high-resolution spectra of C1s can be deconvoluted to three peaks with binding energy of 284.8, 286.2 and 288.5 eV, which were assigned to C–C/C=C, C–N and C=O, respectively; In the high-resolution spectra of N1s, only one peak at 400.3 eV corresponds to C-N in imide ring. Obviously, in the N1s spectrum of PT-COF (Supplementary Figs 8), two peaks were observed at 400.2 and 398.2 eV corresponding to C–N in imide ring and N–(C)2 in triazine ring, respectively. The high-resolution spectra of C1s were divided into four peaks with binding energy of 284.8, 285.9, 286.5 and 287.8 eV, assigned to C–C/C=C, C=N, C–N and C=O, respectively [42,43]. Consequently, above-mentioned results confirm that PI-COFs with abundant C=O groups are successfully synthesised.

Scanning electron microscopy (SEM) and transmission electron microscopy (TEM) revealed that PT-COF exhibited regular morphology of fiber-like structure. (Supplementary Figs 9 and 13). In contrast, PB-COF displayed a uniform nanosheet morphology (Supplementary Figs 11, 14 and 1h). High-resolution transmission electron microscopic (HRTEM) demonstrated high crystallinity of the PB-COF. The 2D layered structure with an interlayer distance of 0.3 nm was clearly observed for PB-COF, corresponded to the (001) plane (Fig. 1i). The thermogravimetric analysis (TGA) revealed that PI-COFs had a high thermal stability up to 550 °C for PB-COF, 545 °C for PT-COF (Supplementary Figs 15). PI-COFs were relatively stable in organic solvents including dimethylformamide, dimethylsulfoxide and tetrahydrofuran (Supplementary Figs 16 and Figs 17). The intensity of crystallinity did not decline significantly, demonstrating that PI-COFs had the extraordinary thermal stability and chemical durability. PT-COF and PB-COF displayed hydrophilic surface with the contact angle of 39.4° and 42.2°, indicating wetting behavior (Supplementary Figs 19). Hydrophilic surface, high crystalline and

excellent stability advantages of PI-COFs are extremely favorable for photocatalysis reaction.
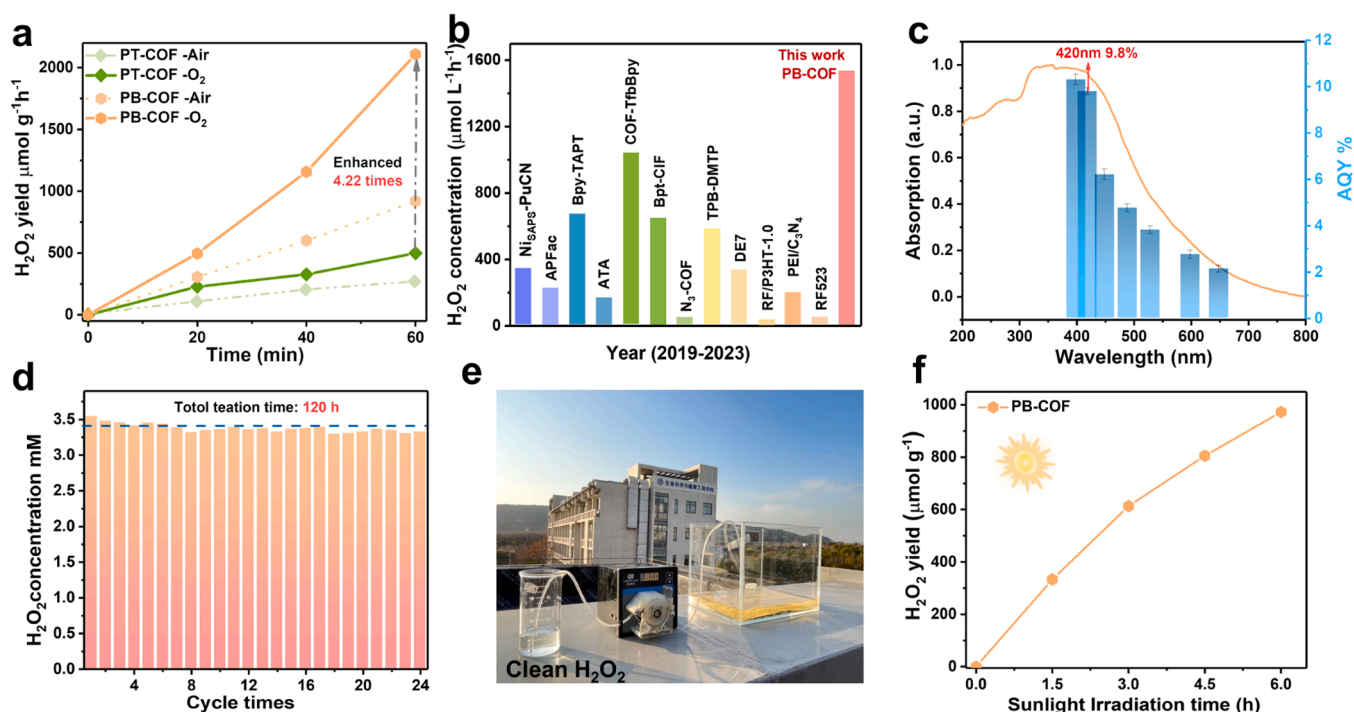
3.2. Photocatalytic H$_2$O$_2$ performance of PI-COFs

The H$_2$O$_2$ photosynthesis performance for as-prepared PI-COFs was evaluated in water and oxygen system under simulated sunlight irradiation. The average H$_2$O$_2$ yield in O$_2$-saturated pure water of PB-COF was 2044 μmol g^{-1} h^{-1}, which was 4.22-fold promotion of PT-COF (484 μmol g^{-1} h^{-1}). PI-COFs photocatalyst also exhibited significant activity for H$_2$O$_2$ photosynthesis in the system of water and air (Fig. 2a). The as-prepared PI-COFs showed outstanding H$_2$O$_2$ production performance without any sacrificial reagents, which exceeded most reported organic photocatalysts (Table S2, Supporting Information and Fig. 2b). The SCC efficiency of PB-COF and PT-COF were measured to be as high as 0.68% and 0.24%, respectively, which was higher than the plants efficiency (0.10%) (Supplementary Figs 20). The apparent quantum efficiency (AQY) experiment of PB-COF was performed via different incident light wavelengths irradiation, acquiring 10.3%, 9.8%, 6.21%, 4.75%, 3.8%, 2.75% and 2.12% at 400, 420, 450, 490, 530, 600 and 650 nm. The AQY results well matched with the trend of the absorption spectrum, implying the importance of light absorption in the photoreaction (Fig. 2c).

As shown in Figure S22 and S23, about 93% of hydrogen peroxide was still present in the reaction system contianing 5 mM, 10 mM and 20 mM H$_2$O$_2$ with PI-COFs photocatalysts after 24 h of continuous light irradiation. These results indicate that PI-COFs photocatalysts do not readily decompose produced H$_2$O$_2$, which facilitate the accumulation of efficient H$_2$O$_2$. Meanwhile, the accumulation amount of H$_2$O$_2$ generated after 8 h irradiation was 8.29 mM for PB-COF, which was more than nearly 4 times higher than for PT-COF (1.87 mM) (Supplementary Figs 25). In addition to the impressive efficiency, PB-COF displayed ultra-durable performance for photosynthesis H$_2$O$_2$ after 24 repeated cycling tests for 120 h, suggesting outstanding photostability of polyimide material (Fig. 2d). According to the FT-IR, XRD, SEM, UV-vis absorption results and EA analysis, no significant structural, morphology and absorption edge change were observed for PI-COFs after the long-term photocatalytic reaction (Supplementary Figs 27–34 and Table S1). Inspired by the remarkable photocatalytic performance, a practical H$_2$O$_2$ generation test was conducted under natural sunlight. To be convenient for separating H$_2$O$_2$ generation, powder PB-COF photocatalyst was immobilized onto nonwoven fabric (20 cm × 15 cm). We dispersed the power PB-COF photocatalyst in ethanol and nafion mixed solution and uniform ultrasonic dispersion. Then the PB-COF mixed solution was drop coating on the nonwoven fabric. The obtained nonwoven fabric was dried in vacuum dry box to remove the possible residual of ethanol. Subsequently, the nonwoven fabric loaded with PB-COF was soaked in water to wash off the unbound powder photocatalyst. Finally, a 300 cm^{-2} PB-COF photocatalyst membrane was successfully prepared. Indeed, PB-COF photocatalyst accumulated the H$_2$O$_2$ yield up to 972.45 μmol g^{-1} (irradiation area: 300 cm^{-2}, accumulative concentration: 311 μmol/L) after 6 h in 200 mL water, revealing extended practical application value (Figs. 2e and 2f). The above results demonstrate that PB-COF efficiently utilize natural sunlight for photosynthesis H$_2$O$_2$.

3.3. The construction of electron-rich carbonyl site

The electronic characteristic of the electron-donating blocks (TAPT or TAPB unit) have a significant impact on the electron distributions of C=O group and molecular dipole of PI-COFs. PB-COF of 0.838 Debye had larger molecular dipole than PT-COF of 0.544 Debye, creating a significant difference in potential between carbonyl group and electron-donating moiety, which provided powerful driving force for charge separation. The carbonyl groups of PB-COF have stronger electron affinity characteristic than the carbonyl groups of PT-COF, indicating PB-

Fig. 2. Photocatalytic performance of PI-COFs for H_2O_2 production from H_2O and O_2 under simulated sunlight irradiation. (a) Typical time course of H_2O_2 production with air or O_2 in 60 min (15 mg powder photocatayst, 20 mL pure water); (b) Performance comparison of PB-COF with other previously reported photocatalysts; (c) Wavelength-dependent AQY results and UV–vis absorption spectra of PB-COF, error bars on mean values are standard deviations of three independent H_2O_2 production tests; (d) Stability test for PB-COF photocatalyst; (e) Photograph of the scaled-up reactor (20 cm × 15 cm× 30 cm) by natural sunlight under air atmosphere in the outdoor environment of Jiang Nan University campus from 10:00 am to 4:00 pm on Aug 12, 2023. The average intensity of sunlight and average temperature was 62.29 mW/cm² and 34.87 ℃; (f) The corresponding photocatalytic H_2O_2 yield for 6 h by PB-COF.

COF more easily accepts photogenerated electrons under photoexcitation (Fig. 3**a**).

We measured electron paramagnetic resonance (ESR) conduction band spectra of PI-COFs to understand charge separation process [44]. PT-COF showed a weak signal at g = 2.003 in the dark, indicating the presence of unpaired electrons. Upon light irradiation, the signal intensity strengthened significantly for PT-COF, showing that more photo-induced electrons were excited from the valence band to the conduction band (Fig. 3**b**). In comparison, PB-COF displayed an obviously stronger EPR signal in the illumination than PT-COF (Fig. 3**c**), demonstrating its superiority in the production of photo-induced electrons. Meanwhile, we also performed photoelectrochemical characterization to explore charge carrier separation in PI-COFs. PB-COF had a smaller charge transfer and transport resistance due to a smaller semicircle, resulting in faster electron transfer kinetics behavior (Supplementary Figs 41). The photocurrent density of PB-COF exhibited significantly higher than PT-COF, which also favored for charge separation in periodic framestructure (Supplementary Figs 42).

To further understand the dynamic behavior of photogenerated charge, surface photovoltage (SPV) spectra was conducted (Supplementary Figs 43). The photovoltage intensity of PB-COF (7.1 μV) was much higher than PT-COF (2.4 μV), showing that PB-COF effectively enhanced charge separation. The charge density of PI-COFs were evaluated via atomic force microscope equipped with Kelvin probe (Fig. 3**d**). The surficial electrostatic potential of PB-COF (154.6 mV) was 2.73 times the values of PT-COF (56.6 mV), which indicated the significantly improved internal electric field. The quenched fluorescence spectra explained that PB-COF had a relatively weak fluorescence signal compared to PT-COF (Supplementary Figs 44), suggesting that PB-COF effectively prevented the electron-hole recombination. What's more, the average relaxation lifetime of PB-COF (2.87 ns) was longer than that of PT-COF (1.37 ns), showing that PB-COF had prolonged lifetime of charge carrier (Fig. 3**e**).

The construction of the built-in electric field in organic semiconductor is the kinetic factor for elevating charge-separation efficiency and accelerating carrier mobility [45,46]. In order to explore the internal electric field of two PI-COFs, we measured photogenerated charge density via the transient photocurrent density and surface voltages by open circuit potential (Supplementary Figs 45). The internal electric field is proportional to the number of charges gathering at the surface of catalyst, by combining transient photocurrent density minus the steady-state values of photocurrent. The results showcased that the photogenerated charge density of PT-COF and PB-COF are 1.58 μC/cm² and 5.11 μC/cm², respectively. The open circuit potential of PT-COF and PB-COF are 0.012 V and 0.041 V, respectively, therefore the internal electric field of two PI-COFs were calculated. It can be found that the internal electric field intensity of PB-COF was 3.32-fold as high as that of PT-COF (Fig. 3**f**). More importantly, benefit from the robust built-in electric field, PB-COF photocatalyst realized efficient charge separation.

In addition, we further have performed time-dependent density functional theory (TD-DFT) calculations with model systems consists of a donor and an acceptor connection in PI-COFs to probe electron transfer and distribution in excited states. The green region represents the accumulation of photogenerated-electrons, while the blue region represents the enrichment of holes. It is obvious that the carbonyl site of PB-COF is nearly 100% enriched with photogenerated electrons in the excited state, compared to carbonyl sites where electrons and holes cluster together on PT-COF (Figs. 3**g** and 3**h**). The above result demonstrated that the introduction of suitable donor effectively tailored the dominant electron occupancy of carbonyl group. The atoms from PMDA-TAPB or PMDA-TAPT molecular form were divided into two sections to discovery the contribution of electron and hole. Fragment 1 and fragment 2 are categorized as PMDA and TAPB or TAPT segments, respectively. For the PB-COF, the contribution of fragment 1 to electron is 99.84% in total, while that of fragment 2 to electron is 0.16%, indicating the electron from TAPB unit transferred to PMDA unit. The
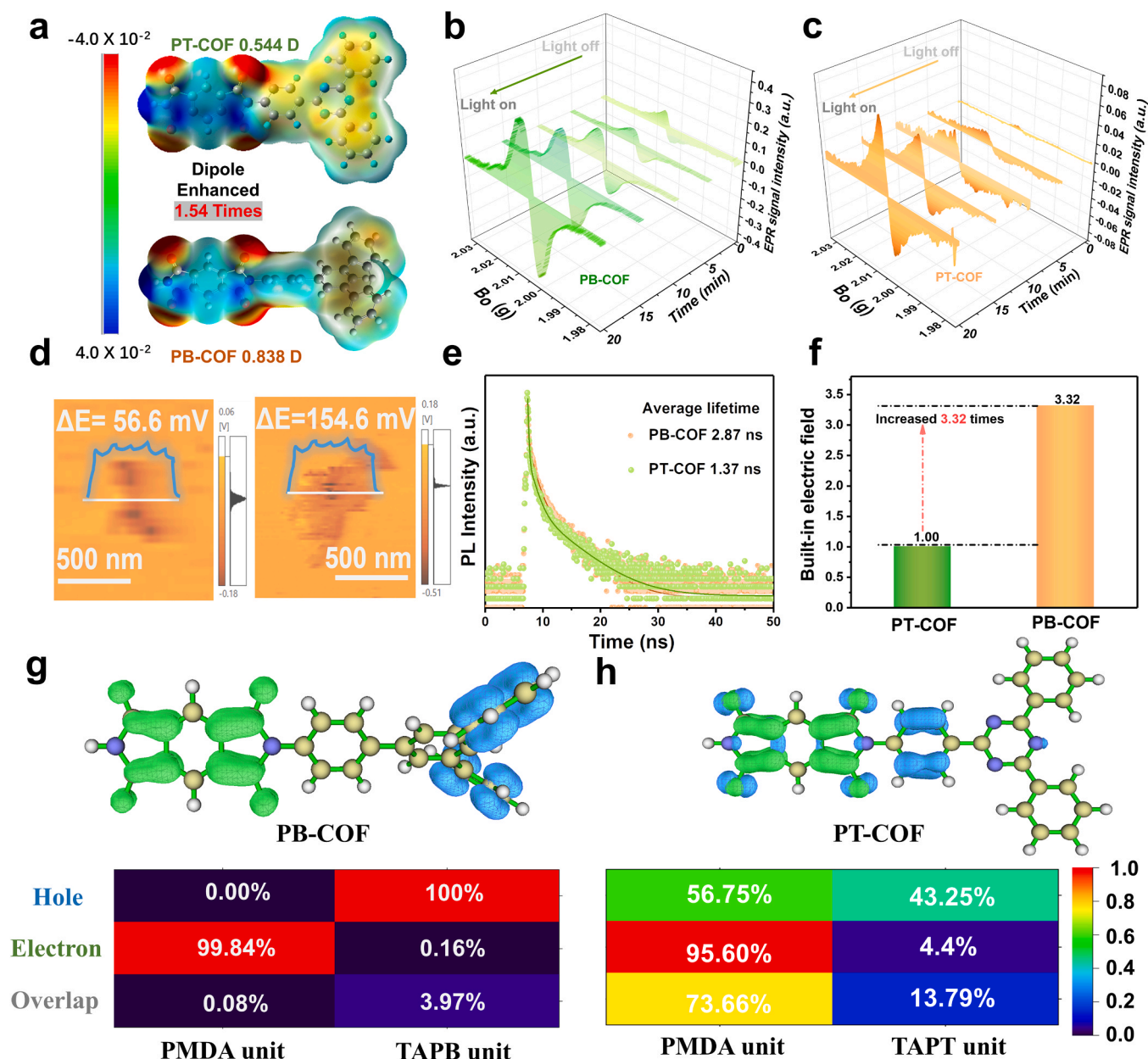
Fig. 3. (a) The molecular electrostatic potential and ground-state dipole moments of PI-COFs; (b) and (c) Electron paramagnetic resonance conduction band electrons spectra of PI-COFs after irradiation (300 W Xe lamp); (d) Surface potentials of PI-COFs detected via atomic force microscope equipped with Kelvin probe; (e) Transient fluorescence spectroscopy spectra of PI-COFs; (f) Internal electric field intensity of PI-COFs; (g) and (h) Real-space hole (blue regions) and electron (green regions) distributions of PMDA-TAPB unit on PB-COF and PMDA-TAPT unit on PT-COF in the excited state (up); The molecular structural formula, the atom and fragment contributions for hole/electron as heat map of PB-COF and PT-COF (down).

overlap of electron-hole is 0.08 and 73.66% on carbonyl site of PB-COF and PT-COF, respectively. Relative to TAPT unit, TAPB unit as electron-donating block is more capable of improving the intermolecular charge separation and suppressing charge recombination, leading to the formation of electron-rich carbonyl site. The electronegative nature of carbonyls on PB-COF and PMDA was investigated (Supplementary Figs 64). The Bader charges for carbonyls group were calculated to be −1.86 in PB-COF and -1.56 in PMDA, suggesting that the electronegativity of carbonyl group on PB-COF was the stronger. Therefore, combining theoretical calculations and comprehensive characterization, we verified that the carbonyl group from PB-COF had the stronger ability to extract electrons, forming electron-rich reductive site upon photoexcitation.

### 3.4. The boosted 2e⁻ ORR mechanism by electron-rich carbonyl site

The optical band gap and band positions are essential for photocatalytic H_2O_2 production. Ultraviolet-visible absorption spectroscopy and Mott-Schottky plots (Supplementary Figs 46 and 47) were executed to confirm the electronic structure of the PI-COFs. The band gap of PB-COF and PT-COF was estimated to be 1.82 and 1.91 eV. The Mott-Schottky plots of PB-COF and PT-COF at varied frequencies (1.2 and 1.8 kHz) exhibited positive slopes. For the obtained PB-COF and PT-COF, E_{CB} was calculated to be −0.43 V and −0.63 V (vs. NHE), and E_{VB} was 1.39 V and 1.28 V (vs. NHE), which provided the thermodynamic driving force to promote the photocatalytic reduction of O_2 to H_2O_2 and oxidation of H_2O to O_2. To investigate the role of the photogenerated electron and hole in PI-COFs, we performed the radical

capture experiments (Supplementary Figs 49). No H_2O_2 was produced under dark. No H_2O_2 also was produced under Ar atmosphere (O_2 removing) or under Ar atmosphere (O_2 removing) with La $(NO_3)_2$ served as electron scavenger, showing that photogenerated hole did not oxidate H_2O into H_2O_2. Additionally, O_2 was detected in Ar-saturated water with 5 mM $NaIO_3$ as an electron-capture reagent with La_2O_3 as pH buffer agent (Supplementary Figs 51) [47]. The rotating ring disk electrode measurement was explored the water oxidation half-reaction of the PI-COFs (Supplementary Figs 52). We set the potential of the Pt ring electrode at -0.23 V or 0.6 V to detect O_2 or H_2O_2 production via water oxidation, respectively. Reduction currents were observed at the Pt ring electrode with the constant potential of -0.23 V, suggesting that PI-COFs were able to generate O_2 via water oxidation. However, when the potential was $+0.6$ V at the Pt ring electrode, an oxidation current was not detected, displaying that PI-COFs were unable to produce H_2O_2 via water oxidation. In the presence of p-benzoquinone as quenching of superoxide radical, the amount of H_2O_2 production was decreased significantly, indicating superoxide radicals played a key role in H_2O_2 production (Supplementary Figs 49).

The O_2 reduction half-reaction of PI-COFs was discussed in detail. We firstly conducted isotopic labeling experiments to investigate the reaction pathway for PI-COFs (Fig. 4a and Supplementary Figs 53) [48]. Isotopic results showed that ^{18}O signals of PB-COF and PT-COF were both detected in the produced H_2O_2 under the case of $H_2^{16}O$ and $^{18}O_2$. The intensity of ^{18}O signal for PB-COF was more higher than PT-COF in the same condition, indicating PB-COF had excellent performance for the photocatalytic reduction of O_2 to H_2O_2. We also demonstrated that the proton source of H_2O_2 produced via 2e⁻ ORR pathway is from H_2O (Supplementary Figs 54). Rotating disk electrode experiments were carried out to determine the average electron transfer number during O_2 reduction process for PI-COFs (Supplementary Figs 55 and 56) [49]. As depicted in Fig. 4**b**, the average electron transfer number was measured to be 1.97 and 2.09 for PT-COF and PB-COF, respectively, indicating PI-COFs had a high two-electron selectivity for ORR process. As we all know, ORR routes contain the direct two-electron ORR process and indirect two-electron ORR process for H_2O_2 synthesis with superoxide radical as the key intermediate [50]. Electron paramagnetic resonance (EPR) was applied to investigate the ORR pathway for PI-COFs (Fig. 4**c**). Superoxide radical was markedly observed for PI-COFs after irradiation 5 min, confirming that PI-COFs generated H_2O_2 via the indirect two-electron ORR process. PB-COF had a stronger signal for superoxide radical than the PT-COF. Furthermore, PB-COF photocatalyst generated more superoxide radical based on the characteristic reaction in O_2-saturated nitro blue tetrazolium (NBT). (Supplementary Figs 57–59). The concentration of superoxide radical generated by PB-COF was 2.27-fold promotion than that of PT-COF verird by the NBT quantitative
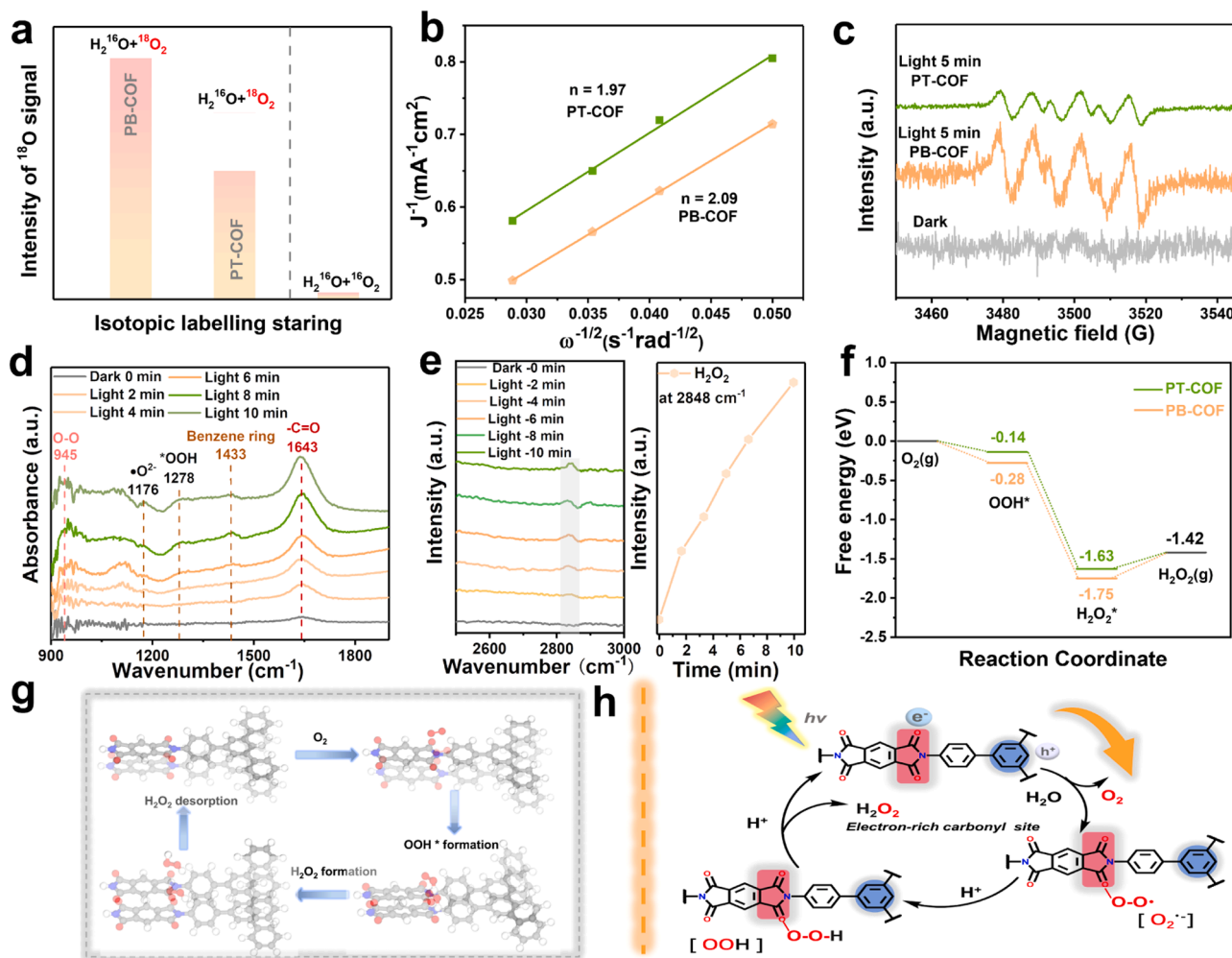
Fig. 4. (a) $^{18}O_2$ Isotopic labeling experiments. The produced $H_2^{18}O_2$ was converted to $H_2^{18}O$; (b) The Koutecky-Levich plots obtained by rotating disk electrode measurements *versus* Ag/AgCl; (c) EPR signals for capturing superoxide radical of PT-COF and PB-COF; (d) *In situ* FTIR spectrum of PB-COF for photosynthetic H_2O_2 production at 900–1850 cm⁻¹ with increasing illumination time and (e) at 2560–3000 cm⁻¹ and corresponding to the peak intensity of H_2O_2 stretching vibrations changes; (f) Gibbs free energy diagram of the C=O group of PI-COFs by the indirect 2e⁻ ORR pathway and (g) corresponding to schematic diagram; (h) Schematic illustration revealing photocatalytic indirect 2e⁻ ORR mechanism on PB-COF.

experiment. These results showed that PB-COF accelerated the photosynthesis of H_2O_2 by promoting the formation of superoxide radical. Obviously, the photogenerated electron and hole in PB-COF were consumed for indiret two-electron ORR process and four-electron WOR process, respectively.

Highly defined structure framework would facilitate the disclose of performance and structure relationship, investigating into photocatalytic mechanism. The reaction intermediate and active site in the photocatalytic process were disclosed by *in situ* diffuse reflectance infrared Fourier transform spectroscopy (DRIFTS) measurements. *In situ* DRIFTS spectra of PI-COFs were continuously recorded at dark / light-O_2 state to explore H_2O_2 production mechanism. As displayed in Fig. 4d, a vibrational peak at about 945 cm^{-1} emerged corresponding to O–O intermediate, suggesting occurrence of the indirect ORR pathway [51]. The vibration signals at approximately 1176 and 1278 cm^{-1} for PB-COF were attributed to superoxide radical and *OOH specie [52,53], which gradually enhanced with the illumination time. Moreover, the signal at 1433 and 1643 cm^{-1} corresponding to phenyl of TAPB unit and C=O of the imide ring were observed gradually strengthened [54,55], respectively. This observation confirms that the C=O group of imide ring undergoes structural stretching vibrations, indicating its serve as reaction active site for photosynthesis H_2O_2. The peak approximately at 2848 cm^{-1} attributed to the typical $(\nu_2 + \nu_6)/2\nu_6$-OH bending feature of H_2O_2 was increasing [56], showing H_2O_2 yield gradually improving (Fig. 4e).

According to the above results, the C=O groups of PI-COFs was served as reductive active center via indirect 2e$^-$ ORR pathway for photocatalytic H_2O_2 production. The formation of *OOH intermediate is recognized as the rate determination step in the indirect 2e$^-$ ORR process [57,58]. What's more, the binding energy of *OOH is influenced by active center. We explored the free energy changes of *OOH adsorbed on the C=O site of PT-COF or PB-COF during indirect 2e$^-$ ORR. As illustrated in Fig. 4f, relative to PT-COF, the C=O site of PB-COF possessed lower energy barriers of *OOH intermediate, indicating the importance of the electron density of C=O group. From a thermodynamic point of view, the electron-rich C=O site had great advantageous for reducing the energy barrier of *OOH formation and H_2O_2 desorption, which improved the catalytic activity. Therefore, the C=O groups with high-electron density facilitate the indirect 2e$^-$ ORR pathway via lower energy barriers, resulting in superior photocatalytic performance.

Based on the experimental and theoretical calculation results, H_2O_2 photosynthesis process over PB-COF photocatalyst is summarized, as explained in Fig. 4h. PB-COF produced more electron and hole pairs under photoirradiation. The photogenerated electrons more efficiently transferred to C=O group from imide ring, while photogenerated holes were localized at TAPB moiety. These orderly separated redox centers in PB-COF further promoted charge separation. Water molecule was oxidized to evolve O_2 by the accumulated holes at the benzene ring. Meanwhile, O_2 adsorbed on C=O group transformed to the superoxide radical by combining photogenerated electron. The ·O^{2-} intermediate species subsequently further coupled hydrogen protons from H_2O molecule at the C=O site to transform into H_2O_2.

4. Conclusions

In summary, we developed PI-COFs based photocatalysts with carbonyl group site of different electron-trapping ability for high-efficiency H_2O_2 production. The PB-COF with high electron-trapping capacity for carbonyl site displayed a extraordinary SCC of 0.68% and AQY of 9.8% at 420 nm, representing advanced polymer-based photocatalysts. More importantly, we successfully established the robust built-in electric field through larger molecular dipole in framework structure to elevate charge separation and directional transfer efficiency, leading to enhanced the electron density of carbonyl group with strong electron affinity. Comprehensive *in-situ* spectroscopic studies correlated with theoretical calculations, we unveiled electron-rich carbonyl site is

crucial for significantly boosting kinetics for 2e$^-$ ORR, improving photocatalysis performance via lowering the energy barrier of *OOH intermediate. Our works not only provide a new strategy for the design of active site by regulating the electron density, but also offer advanced insights for imide-based COFs to efficient photocatalytic solar energy conversion.

CRediT authorship contribution statement

Bing Liu: Methodology, Formal analysis. **Yuming Dong:** Writing – review & editing, Writing – original draft, Supervision, Investigation, Funding acquisition, Conceptualization. **Wenwen Chi:** Writing – review & editing, Writing – original draft, Investigation, Conceptualization. **Chengsi Pan:** Supervision. **Hui Zhao:** Supervision. **Jiawei Zhang:** Methodology. **Xinyu Sun:** Formal analysis. **Yujie Ling:** Investigation. **Yongfa Zhu:** Supervision, Funding acquisition.

Declaration of Competing Interest

The authors declare that they have no known competing financial interests or personal relationships that could have appeared to influence the work reported in this paper.

Data Availability

Data will be made available on request.

Acknowledgements

Appendix A. Supporting information

Supplementary data associated with this article can be found in the online version at doi:10.1016/j.apcatb.2024.124077.

References

[1] Q. Zhou, Y. Guo, Y. Zhu, Photocatalytic sacrificial H_2 evolution dominated by micropore-confined exciton transfer in hydrogen-bonded organic frameworks, Nat. Catal. 6 (2023) 574–584.

[2] Y. Wang, A. Vogel, M. Sachs, R.S. Sprick, L. Wilbraham, S.J.A. Moniz, R. Godin, M.A. Zwijnenburg, J.R. Durrant, A.I. Cooper, J. Tang, Current understanding and challenges of solar-driven hydrogen generation using polymeric photocatalysts, Nat. Energy 4 (2019) 746–760.

[3] K.P. Bryliakov, Catalytic Asymmetric oxygenations with the environmentally benign oxidants H_2O_2 and O_2, Chem. Rev. 117 (2017) 11406–11459.

[4] Y. Sun, L. Han, P. Strasser, A comparative perspective of electrochemical and photochemical approaches for catalytic H_2O_2 production, Chem. Soc. Rev. 49 (2020) 6605–6631.

[5] A. Gopakumar, P. Ren, J. Chen, B.V. Manzolli Rodrigues, H.Y. Vincent Ching, A. Jaworski, S.V. Doorslaer, A. Rokicinska, P. Kustrowski, G. Barcaro, S. Monti, A. Slabon, S. Das, Lignin-supported heterogeneous photocatalyst for the direct generation of H_2O_2 from Seawater, J. Am. Chem. Soc. 144 (2022) 2603–2613.

[6] Q. Wu, J. Cao, X. Wang, Y. Liu, Y. Zhao, H. Wang, Y. Liu, H. Huang, F. Liao, M. Shao, Z. Kang, A metal-free photocatalyst for highly efficient hydrogen peroxide photoproduction in real seawater, Nat. Commun. 12 (2021) 483.

[7] H. Hou, X. Zeng, X. Zhang, Production of hydrogen peroxide by photocatalytic processes, Angew. Chem. 59 (2020) 17356–17376.

[8] H. Cheng, J. Cheng, L. Wang, H. Xu, Reaction pathways toward sustainable photosynthesis of hydrogen peroxide by polymer photocatalysts, Chem. Mater. 34 (2022) 4259–4273.

[9] W. Yu, C. Hu, L. Bai, N. Tian, Y. Zhang, H. Huang, Photocatalytic hydrogen peroxide evolution: What is the most effective strategy? Nano Energy 104 (2022) 107906.

[10] Z. Yong, T. Ma, Solar-to-H₂O₂ Catalyzed by covalent organic frameworks, Angew. Chem. (2023) e202308980.

[11] G. Pan, X. Hou, Z. Liu, C. Yang, J. Long, G. Huang, J. Bi, Y. Yu, L. Li, The Hydration-initiated pathway of water oxidation over photoexcited covalent organic frameworks, ACS Catal. 12 (2022) 14911.

[12] S. Wu, C. Li, Y. Wang, Y. Zhuang, Y. Pan, N. Wen, S. Wang, Z. Zhang, Z. Ding, R. Yuan, W. Dai, X. Fu, J. Long, The Keto-switched photocatalysis of reconstructed covalent organic frameworks for efficient hydrogen evolution, Angew. Chem. 62 (2023) e202309026.

[13] M.S. Lohse, T. Bein, Covalent organic frameworks: structures, synthesis, and applications, Adv. Funct. Mater. 28 (2018) 1705553.

[14] Z. Xiong, B. Sun, H. Zou, R. Wang, Q. Fang, Z. Zhang, S. Qiu, Amorphous-to-crystalline transformation: general synthesis of hollow structured covalent organic frameworks with high crystallinity, J. Am. Chem. Soc. 144 (2022) 6583–6593.

[15] C. Xing, P. Mei, Z. Mu, B. Li, X. Feng, Y. Zhang, B. Wang, Enhancing enzyme activity by the modulation of covalent interactions in the confined channels of covalent organic frameworks, Angew. Chem. 61 (2022) e202201378.

[16] Y. Shiraishi, T. Takii, T. Hagi, S. Mori, Y. Kofuji, Y. Kitagawa, S. Tanaka, S. Ichikawa, T. Hirai, Resorcinol-formaldehyde resins as metal-free semiconductor photocatalysts for solar-to-hydrogen peroxide energy conversion, Nat. Mater. 18 (2019) 985–993.

[17] Z. Teng, Q. Zhang, H. Yang, K. Kato, W. Yang, Y.-R. Lu, S. Liu, C. Wang, A. Yamakata, C. Su, B. Liu, T. Ohno, Atomically dispersed antimony on carbon nitride for the artificial photosynthesis of hydrogen peroxide, Nat. Catal. 4 (2021) 374–384.

[18] C. Qin, X. Wu, L. Tang, X. Chen, M. Li, Y. Mou, B. Su, S. Wang, C. Feng, J. Liu, X. Yuan, Y. Zhao, H. Wang, Dual donor-acceptor covalent organic frameworks for hydrogen peroxide photosynthesis, Nat. Commun. 14 (2023) 5238.

[19] D. Chen, W. Chen, Y. Wu, L. Wang, X. Wu, H. Xu, L. Chen, Covalent organic frameworks containing dual O₂ reduction centers for overall photosynthetic hydrogen peroxide production, Angew. Chem. 62 (2023) e202217479.

[20] Y. Luo, B. Zhang, C. Liu, D. Xia, X. Ou, Y. Cai, Y. Zhou, J. Jiang, B. Han, Sulfone-modified covalent organic frameworks enabling efficient photocatalytic hydrogen peroxide generation via one-step two-electron O₂ reduction, Angew. Chem. 62 (2023) e202305355.

[21] Q. Liao, Q. Sun, H. Xu, Y. Wang, Y. Xu, Z. Li, J. Hu, D. Wang, H. Li, K. Xi, Regulating relative nitrogen locations of diazene functionalized covalent organic frameworks for overall H₂O₂ Photosynthesis, Angew. Chem. 62 (2023) e202310556.

[22] F. Hao, C. Yang, X. Lv, F. Chen, S. Wang, G. Zheng, Q. Han, Photo-driven quasi-topological transformation exposing highly active nitrogen cation sites for enhanced photocatalytic H₂O₂ Production, Angew. Chem. 62 (2023) e202315456.

[23] J.Y. Yue, L.P. Song, Y.F. Fan, Z.X. Pan, P. Yang, Y. Ma, Q. Xu, B. Tang, Thiophene-containing covalent organic frameworks for overall photocatalytic H₂O₂ synthesis in water and seawater, Angew. Chem. 62 (2023) e202309624.

[24] Y.L. Sun, J.H. Huang, Improvement of the selectivity for hydrogen peroxide production via the synergy of TiO₂ and graphene, Chin. J. Struct. Chem. 41 (2022) 2203085.

[25] D. Tan, R. Zhuang, R. Chen, M. Ban, W. Feng, F. Xu, X. Chen, Q. Wang, Covalent organic frameworks enable sustainable solar to hydrogen peroxide, Adv. Funct. Mater. (2023) 2311655.

[26] F. Tan, Y. Zheng, Z. Zhou, H. Wang, X. Dong, J. Yang, Z. Ou, H. Qi, W. Liu, Z. Zheng, X. Chen, Aqueous synthesis of covalent organic frameworks as photocatalysts for hydrogen peroxide production, CCS Chem. 4 (2022) 3751–3761.

[27] L. Liu, M.-Y. Gao, H. Yang, X. Wang, X. Li, A.I. Cooper, Linear conjugated polymers for solar-driven hydrogen peroxide production: The importance of catalyst stability, J. Am. Chem. Soc. 143 (2021) 19287–19293.

[28] W. Zhao, P. Yan, B. Li, M. Bahri, L. Liu, X. Zhou, R. Clowes, N.D. Browning, Y. Wu, J.W. Ward, A.I. Cooper, Accelerated synthesis and discovery of covalent organic framework photocatalysts for hydrogen peroxide production, J. Am. Chem. Soc. 144 (2022) 9902–9909.

[29] T. Zhong, S. Tang, W. Huang, W. Liu, H. Zhao, L. Hu, S. Tian, C. He, Cu nanocrystals coupled with poly (heptazine imide) for synergistically enhanced photocatalytic CH₃SH elimination: facet engineering strengthened electron pump effect, Appl. Catal. B: Environ. 343 (2024) 123476.

[30] Y. Zhang, Z. Huang, B. Ruan, X. Zhang, T. Jiang, N. Ma, F.C. Tsai, Design and synthesis of polyimide covalent organic frameworks, Macromol. Rapid Commun. 41 (2020) e2000402.

[31] L. Jiang, Y. Tian, T. Sun, Y. Zhu, H. Ren, X. Zou, Y. Ma, K.R. Meihaus, J.R. Long, G. Zhu, A crystalline polyimide porous organic framework for selective adsorption of acetylene over ethylene, J. Am. Chem. Soc. 140 (2018) 15724–15730.

[32] L. Li, Y.J. Yin, J.P. Hei, X.J. Wan, M.L. Li, Y. Cui, Molecular engineering of aromatic imides for organic secondary batteries, Small 17 (2021) e2005752.

[33] Z. Luo, L. Liu, J. Ning, K. Lei, Y. Lu, F. Li, J. Chen, A microporous covalent-organic framework with abundant accessible carbonyl groups for lithium-ion batteries, Angew. Chem. 57 (2018) 9443–9446.

[34] M.A. Kobaisi, S.V. Bhosale, K. Latham, A.M. Raynor, S.V. Bhosale, Functional naphthalene diimides: synthesis, properties, and applications, Chem. Rev. 116 (2016) 11685–11796.

[35] Y. Wan, L. Wang, H. Xu, X. Wu, J. Yang, A simple molecular design strategy for two-dimensional covalent organic framework capable of visible-light-driven water splitting, J. Am. Chem. Soc. 142 (2020) 4508–4516.

[36] Z. Song, H. Zhan, Y. Zhou, Polyimides: promising energy-storage materials, Angew. Chem. 49 (2010) 8444–8448.

[37] Q. Fang, Z. Zhuang, S. Gu, R.B. Kaspar, J. Zheng, J. Wang, S. Qiu, Y. Yan, Designed synthesis of large-pore crystalline polyimide covalent organic frameworks, Nat. Commun. 5 (2014) 4503.

[38] X. Chen, Q. Dang, R. Sa, L. Li, L. Li, J. Bi, Z. Zhang, J. Long, Y. Yu, Z. Zou, Integrating single Ni sites into biomimetic networks of covalent organic frameworks for selective photoreduction of CO₂, Chem. Sci. 11 (2020) 6915–6922.

[39] H. Duan, K. Li, M. Xie, J.M. Chen, H.G. Zhou, X. Wu, G.H. Ning, A.I. Cooper, D. Li, Scalable synthesis of ultrathin polyimide covalent organic framework nanosheets for high-performance lithium-sulfur batteries, J. Am. Chem. Soc. 143 (2021) 19446–19453.

[40] Z. Wang, Y. Zhang, T. Wang, E. Lin, T. Wang, Y. Chen, P. Cheng, Z. Zhang, Modulating the interlayer stacking of covalent organic frameworks for efficient acetylene separation, Small 19 (2023) e2303684.

[41] M.R. Liebl, J. Senker, Microporous functionalized triazine-based polyimides with high CO₂ capture capacity, Chem. Mater. 25 (2013) 970–980.

[42] N. Zhao, J.-M. Liu, F.-E. Yang, S.-W. Lv, J. Wang, S. Wang, Easy green construction of a universal sensing platform based on crystalline polyimide covalent organic frameworks with sensitive fluorescence response to metal ions and antibiotics, ACS Appl. Bio Mater. 4 (2020) 995–1002.

[43] Y. Kofuji, S. Ohkita, Y. Shiraishi, H. Sakamoto, S. Tanaka, S. Ichikawa, T. Hirai, Graphitic carbon nitride doped with biphenyl diimide: efficient photocatalyst for hydrogen peroxide production from water and molecular oxygen by sunlight, ACS Catal. 6 (2016) 7021–7029.

[44] J. Yang, S. Ghosh, J. Roeser, A. Acharjya, C. Penschke, Y. Tsutsui, J. Rabeah, T. Wang, S.Y. Djoko Tameu, M.Y. Ye, J. Gruneberg, S. Li, C. Li, R. Schomacker, R. Van De Krol, S. Seki, P. Saalfrank, A. Thomas, Constitutional isomerism of the linkages in donor-acceptor covalent organic frameworks and its impact on photocatalysis, Nat. Commun. 13 (2022) 6317.

[45] J. Xu, W. Li, W. Liu, J. Jing, K. Zhang, L. Liu, J. Yang, E. Zhu, J. Li, Y. Zhu, Efficient photocatalytic hydrogen and oxygen evolution by side-group engineered benzodiimidazole oligomers with strong built-in electric fields and short-range crystallinity, Angew. Chem. 61 (2022) e202212243.

[46] D. Liu, X. Yang, P. Chen, X. Zhang, G. Chen, Q. Guo, H. Hou, Y. Li, Rational design of PDI-based linear conjugated polymers for highly effective and long-term photocatalytic oxygen evolution, Adv. Mater. 35 (2023) e2300655.

[47] H. Cheng, H. Lv, J. Cheng, L. Wang, X. Wu, H. Xu, Rational design of covalent heptazine frameworks with spatially separated redox centers for high-efficiency photocatalytic hydrogen peroxide production, Adv. Mater. 34 (2022) e2107480.

[48] Y. Zhang, C. Pan, G. Bian, J. Xu, Y. Dong, Y. Zhang, Y. Lou, W. Liu, Y. Zhu, H₂O₂ generation from O₂ and H₂O on a near-infrared absorbing porphyrin supramolecular photocatalyst, Nat. Energy 8 (2023) 361–371.

[49] H. Yan, M. Shen, Y. Shen, X.D. Wang, W. Lin, J. Pan, J. He, Y.X. Ye, X. Yang, F. Zhu, J. Xu, J. He, G. Ouyang, Spontaneous exciton dissociation in organic photocatalyst under ambient conditions for highly efficient synthesis of hydrogen peroxide, PNAS 119 (2022) e2202913119.

[50] M. Kou, Y. Wang, Y. Xu, L. Ye, Y. Huang, B. Jia, H. Li, J. Ren, Y. Deng, J. Chen, Y. Zhou, K. Lei, L. Wang, W. Liu, H. Huang, T. Ma, Molecularly engineered covalent organic frameworks for hydrogen peroxide photosynthesis, Angew. Chem. 61 (2022) e202200413.

[51] C. Wu, Z. Teng, C. Yang, F. Chen, H.B. Yang, L. Wang, H. Xu, B. Liu, G. Zheng, Q. Han, Polarization engineering of covalent triazine frameworks for highly efficient photosynthesis of hydrogen peroxide from molecular oxygen and water, Adv. Mater. 34 (2022) 2110266.

[52] J.Y. Yue, L.P. Song, Y.F. Fan, Z.X. Pan, P. Yang, Y. Ma, Q. Xu, B. Tang, Thiophene-containing covalent organic frameworks for overall photocatalytic H₂O₂ synthesis in water and seawater, Angew. Chem. 62 (2023) e202309624.

[53] C. Zhao, X. Wang, Y. Yin, W. Tian, G. Zeng, H. Li, S. Ye, L. Wu, J. Liu, Molecular level modulation of anthraquinone-containing resorcinol-formaldehyde resin photocatalysts for H₂O₂ production with exceeding 1.2% efficiency, Angew. Chem. 62 (2023) e202218318.

[54] M. Kou, Y. Wang, Y. Xu, L. Ye, Y. Huang, B. Jia, H. Li, J. Ren, Y. Deng, J. Chen, Y. Zhou, K. Lei, L. Wang, W. Liu, H. Huang, T. Ma, Molecularly engineered covalent organic frameworks for hydrogen peroxide photosynthesis, Angew. Chem. 61 (2022) e202200413.

[55] X.X. Luo, W.H. Li, H.J. Liang, H.X. Zhang, K.D. Du, X.T. Wang, X.F. Liu, J.P. Zhang, X.L. Wu, Covalent organic framework with highly accessible carbonyls and pi-cation effect for advanced potassium-Ion batteries, Angew. Chem. 61 (2022) e202117661.

[56] L. Chen, L. Wang, Y. Wan, Y. Zhang, Z. Qi, X. Wu, H. Xu, Acetylene and diacetylene functionalized covalent triazine frameworks as metal-free photocatalysts for hydrogen peroxide production: a new two-electron water oxidation pathway, Adv. Mater. 32 (2020) e1904433.

[57] X. Zhou, Y. Min, C. Zhao, C. Chen, M.K. Ke, S.L. Xu, J.J. Chen, Y. Wu, H.Q. Yu, Constructing sulfur and oxygen super-coordinated main-group electrocatalysts for selective and cumulative H₂O₂ production, Nat. Commun. 15 (2024) 193.

[58] T. Yang, Y. Jin, Y. Wang, A. Kong, Y. Chen, Y. Zou, C. Liu, G. Wei, C. Yu, Covalent furan-benzimidazole-linked polymer hollow fiber membrane for clean and efficient photosynthesis of hydrogen peroxide, Adv. Funct. Mater. 33 (2023) 2300714.